CrossMark

Graphene-Supported Cobalt(III) Complex of a Tetraamidomacrocyclic Ligand for Oxygen Reduction Reaction

Hunter A. Wayland[1] · Susan N. Boury[1] · Yahya Albkuri[1] · Fumiya Watanabe[2] · Alexandru S. Biris[2] · Charlette M. Parnell[2] · Anindya Ghosh[1]

Abstract

Polymer electrolyte membrane fuel cells (PEMFCs) are at the cusp of providing large scale energy solutions, yet challenges in developing high performance, durable, and cost effective platinum catalyst alternatives continue to impede commercialization efforts. A graphene-supported cobalt(III) catalyst nanocomposite was prepared and investigated for the first time as a potential cathode material for PEMFCs. The material was characterized using a variety of microscopy and spectroscopy techniques, and the electrochemical performance was assessed using voltammetry equipment. A peak potential at -0.088 V versus standard hydrogen electrode was observed by cyclic voltammetry during oxygen reduction reaction (ORR). The material was found to reduce oxygen via a four-electron process in both acidic and alkaline pH conditions, with rotating disk electrode and rotating ring disk electrode studies revealing the ORR to occur via 3.60 and 3.86 electrons at pH 2, respectively. A rate constant of 9.78×10^6 mol^{-1} s^{-1} was observed for the cobalt(III) catalyst/graphene complex in acidic conditions, and a mechanism has been proposed based on these results.
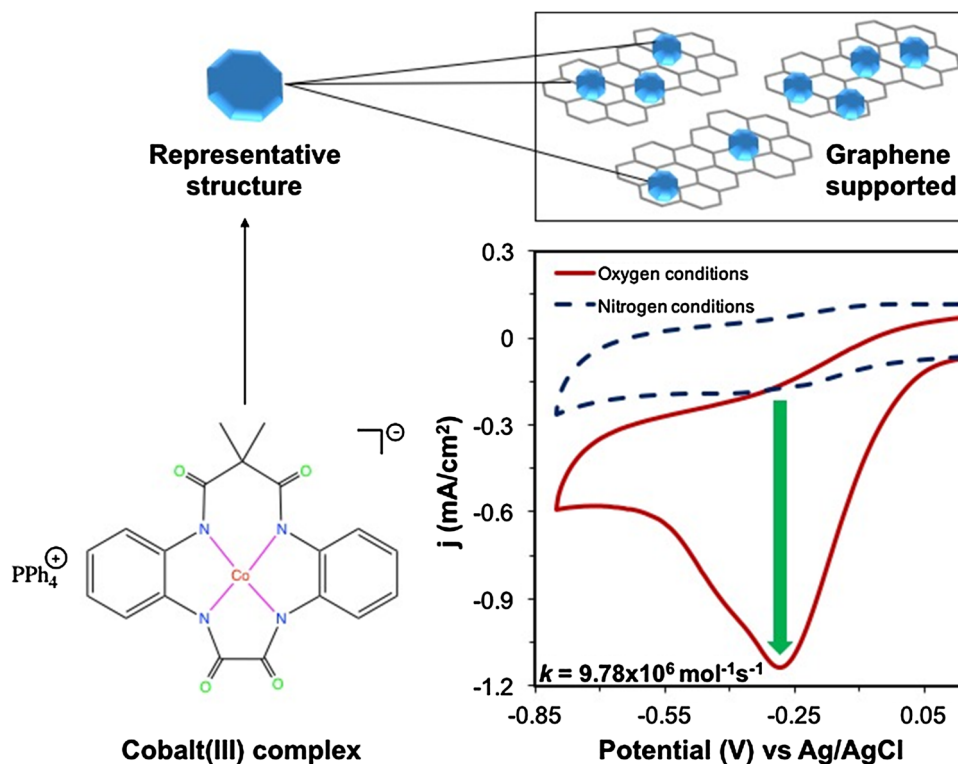
✉ Charlette M. Parnell
cmfelton@ualr.edu

✉ Anindya Ghosh
axghosh@ualr.edu

1 Department of Chemistry, University of Arkansas at Little Rock, 2801 South University Avenue, Little Rock, AR 72204, USA

2 Center for Integrative Nanotechnology Sciences, University of Arkansas at Little Rock, 2801 South University Avenue, Little Rock, AR 72204, USA

Graphical Abstract

An economic, non-precious cobalt(III) complex supported on graphene successfully reduced oxygen at a high rate in cathodic fuel cell applications.

Keywords Cobalt catalyst · Oxygen reduction reaction · Fuel cells · Cathode material · Alternative energy · Graphene

1 Introduction

Technological advances over the course of the past decade have allowed for the production and application of fuel cells on a commercial level, benefiting not only the environment but also holding promise for economic and political sectors in terms of cleaner energy, lower fuel cost, and the opportunity for liberation from dependence on fossil fuels [1]. Compared to traditional combustion engines, fuel cells are more efficient in practice due to their lower operating temperatures and fewer irreversible heat rejection processes; furthermore, there are various advantages associated with using fuel cells such as their high reliability, tremendous power density, quiet operation, and ability to remotely monitor status conditions [2, 3]. Numerous categories of fuel cells exist on the market, including alkaline, biofuel, solid oxide, microbial, direct alcohol, and polymer electrolyte membrane (PEM) [4–11]. Among these, classification may be based on the fuel source, with some such as biofuel and direct methanol operating on low molecular weight alcohols, and others including PEM and alkaline relying on hydrogen as

fuel [12]. In polymer electrolyte membrane fuel cells (PEMFCs), which are among the most commercializable alternative energy solutions available today, hydrogen serves as the fuel and oxygen as the oxidant, with oxidation of hydrogen occurring at the anode and reduction of oxygen occurring at the cathode [13]. Herein lies perhaps the most superior feature of PEMFCs over traditional engines, such as those used in automobiles: they have essentially zero emissions, which is highly desirable with the current challenges humanity is facing regarding anthropogenic climate change, and particularly carbon emissions [14, 15].

Traditionally, platinum and platinum alloy materials are used as electrode materials in PEMFCs, but with the often volatile prices of platinum rising higher due to increasingly scarce supply, research into alternative materials has been driven to develop more affordable materials for oxygen reduction at the cathode [16]. Currently, over half of the cost associated with setting up a PEMFC is due to the use of platinum in both electrodes of the fuel cell; therefore, finding a viable alternative is of great importance if fuel cells are to be marketed widely, such as for the automotive industry

[17]. The kinetics of ORR particularly, which occurs at the cathode, is much slower than the hydrogen oxidation occurring at the anode, and this translates to a greater platinum load required at the cathode to overcome efficiency losses [18]. Other than prohibitive expense, platinum catalysts are highly susceptible to poisoning (which leads to performance degradation) by numerous fuel and air contaminants including various hydrocarbons and sulfur/phosphate compounds but most notably by methanol and carbon monoxide [19–22]. There exist a variety of approaches to developing hardy platinum alternatives, including metal oxides and phosphates, carbon-supported metal complexes, and even standalone heteroatom-doped carbon materials [23–28]. Transition-metal, or otherwise non-precious, based MN_4 complexes are of particular interest as these may be produced much more cheaply than platinum materials and may be modeled after highly efficient biological oxygen reduction systems [29–31]. Carbon supports are further able to enhance the activity of electrochemical catalysts by providing an electron conducting surface and protection from fuel and air contaminants as well as enabling consistent catalyst dispersion. Furthermore, these materials may be produced from biomass residues making the production of alternative cathode materials even less expensive [32–34]. Various carbon support materials have been investigated, including carbon nanotubes (both single- and multi-walled), graphitic nanofibers, carbon black, and graphene sheets [35]. The harsh cathode conditions present in fuel cells are as detrimental to carbon support materials as they are to catalysts, and less structured materials such as carbon black are quick to oxidize; therefore, the most stable materials are nanoscale, and these are often most effective in circumnavigating cathode corrosion issues [36, 37].

Various amidomacrocyclic catalyst materials for fuel cell and other applications have been previously investigated, and several cobalt (Co) complexes are among these [38–42]. In this publication, we report for the first time the synthesis, characterization, and ORR activity of a novel Co(III) amidomacrocyclic 5*H*-dibenzo[*b,h*] [1, 4, 7, 10] tetraazacyclotridecine-6,7,14,16(15*H*,17*H*)-tetrone,8,13-dihydro-15,15-dimethyl catalyst-graphene nanocomposite material to be used as a platinum alternative cathode coating in fuel cells. The catalyst itself was characterized using Fourier-transform infrared spectroscopy (FT-IR), electrospray ionization mass spectrometry (ESI-MS), and ultraviolet–visible spectroscopy (UV–Vis). Scanning electron microscopy (SEM) and transmission electron microscopy (TEM) in addition to scanning-transmission electron microscopy-coupled-elemental dispersive analysis (STEM-EDS) were performed on the nanocomposite to assess the surface morphology and distribution of elements within the material. X-ray diffraction analysis (XRD) and X-ray photoelectron spectroscopy (XPS) were employed to assess the states of both the carbon nanomaterial as well as the other elements found in the material. Evaluation of electrochemical properties was accomplished using cyclic voltammetry (CV), rotating disk electrode voltammetry (RDE), and rotating ring disk voltammetry (RRDE). These electrochemical techniques also allowed for elucidation of the mechanism via which the nanocomposite performs ORR. The nanocomposite was found to perform ORR at a peak potential of −0.088 V (versus standard hydrogen electrode; SHE) and this process was further revealed to proceed through the more desirable four-electron process in both acidic and alkaline conditions. The rate constant observed in acidic conditions is 9.78×10^6 mol^{-1} s^{-1}, which is one of the highest reported rate constants for cobalt ORR catalysts currently found in the literature, and the mechanism proceeds via 3.60 electrons. Based on these performance results in acidic conditions, this material has definite potential for application in acidic PEMFCs; furthermore, evaluation of the nanocomposite behavior in alkaline conditions demonstrates that the material may find application in other types of fuel cells as well. A schematic illustration of the developed material and its application within a general PEMFC is presented in Fig. 1.

2 Experimental

2.1 General Information

The chemicals used for experimentation were purchased from VWR International, Sigma-Aldrich, or Acros Organics unless otherwise stated. Ultrahigh purity nitrogen gas (N_2) and oxygen gas (O_2) were purchased from North Little Rock Welding Supply. Multi-walled carbon nanotubes (MWCNTs) were obtained from Bayer Materials Science (Baytubes C150P RD SAM) and used without modification. Graphene was obtained from Angstron Materials (97% purity N002-PDR graphene powder) and used as received. Phosphate buffer solutions of pH 2 and 9 were prepared following a documented procedure [43]. FT-IR spectrum was obtained with a Thermo Scientific Nicolet 6700 FT-IR spectrometer. ESI-MS was collected using an Agilent 1100 Series MSD Trap VL spectrometer. The UV–Vis spectrum was performed on a Varian Cary 5000 UV–Vis–NIR spectrophotometer. CV studies, as well as RDE and RRDE studies were performed at 25 °C using a Pine Instrument biopotentiostat Model AFCBP1. SEM was performed using a JEOL SEM (JSM 7000F), TEM was done by JEOL JEM 2100F equipped with a field emission gun at 80 kV acceleration voltage, and STEM was carried out using a JEOL TEM (JEM 2100F) with an EDS X-ray detector (EDAX Corporation) for elemental analysis. XRD was performed using Brüker D8 Discover XRD system in the 2θ range of 7.9°–82.3° with a step size of 0.02° at a standard potential
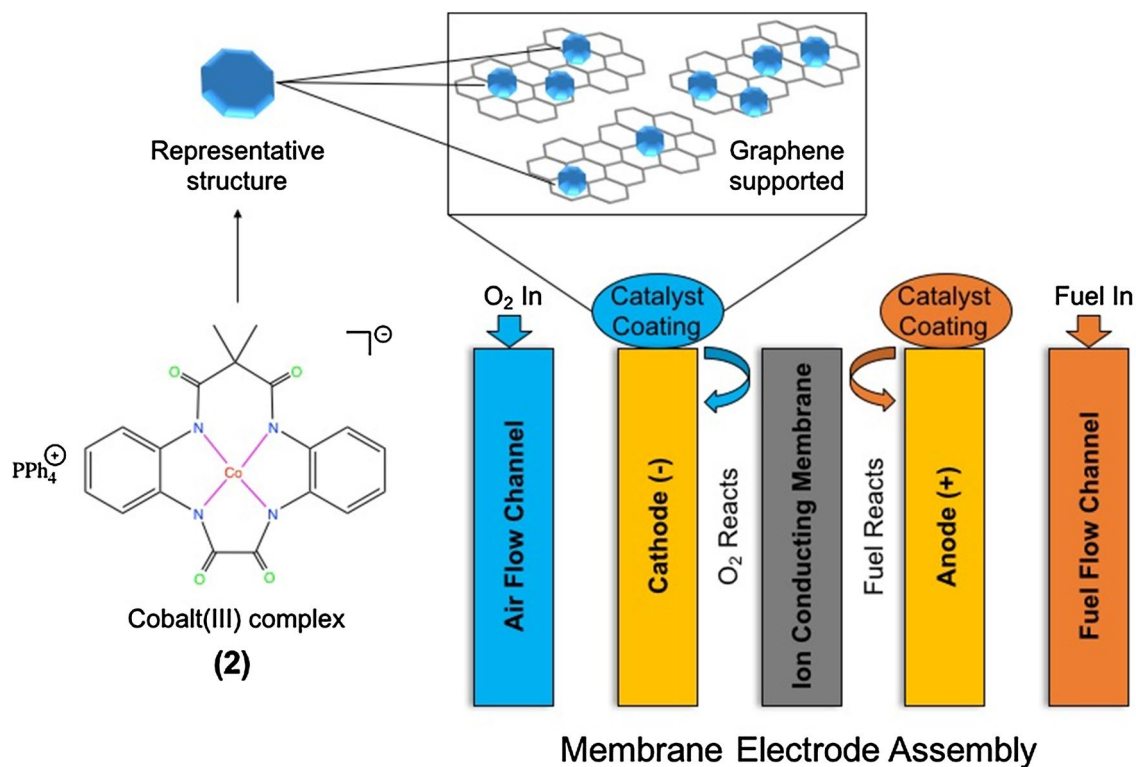
Fig. 1 Application of graphene-supported Co(III) complex as non-precious fuel cell cathode coating for ORR

and current of 40 kV and 40 mA, respectively, on a Cu source with Kα line equal to 0.154 nm. XPS was analyzed with a Thermo Scientific K-Alpha instrument with X-ray spot size of 200 μm and monochromatic Al Kα radiation of 1486.7 eV. The base pressure in the analysis chamber was typically 1×10^{-9} mbar. Samples were mounted on a stage using double-sided tape and spectra were collected with the charge neutralization flood gun on (analysis pressure typically 2×10^{-7} mbar). Thermo Scientific Advantage XPS software was used to process the collected data. Spectral charge correction performed using primary C1s peak set to 284.8 eV. Mixed Gaussian–Lorentzian peak shapes and Shirley/Smart type background subtraction were used for peak fitting and analysis. Elemental analysis was carried out through Midwest MicroLab in Indianapolis, IN, USA.

2.2 Synthesis of Co(III) Complex

The ligand was synthesized according to a previously published procedure (see Figure S1, Supporting Information) [41, 42]. Following synthesis, the metal complex was obtained according to Figure S2 (Supporting Information). The amidomacrocyclic ligand, 5*H*-dibenzo[*b,h*] [1, 4, 7, 10] tetraazacyclotridecine-6,7,14,16(15*H*,17*H*)-tetrone,8,13-dihydro-15,15-dimethyl (**1**, 200 mg, 0.59 mmol) was purged with N_2 gas and dissolved in

20 mL anhydrous tetrahydrofuran in a 100-mL Schlenk flask under an N_2 atmosphere. This was then cooled to 0 °C in an ice bath before adding *n*-butyllithium (0.98 mL, 2.4 mmol of 2.5 M in hexanes) to the solution and stirring for 20 min. Anhydrous Co(II) chloride (77 mg, 0.59 mmol) was then added to the solution and the reaction mixture was stirred overnight at room temperature. To yield the Co(III) complex, the reaction vessel was opened to the air for several hours to oxidize the metal center from Co(II) to Co(III), after which the solvent was removed using a rotary evaporator. The product was further dried in a vacuum oven overnight (249 mg, 74.6% yield). After drying, and following a published literature procedure, the complex was converted from lithium (Li^+) salt to tetraphenylphosphonium (PPh_4^+) salt by dissolving the lithium salt in deionized water, filtering to remove insoluble, and adding a molar equivalent amount of PPh_4Cl, causing the complex to become insoluble in the aqueous solution [44]. The salt was collected by vacuum filtration and dried once more under vacuum. Co(III) complex (**2**) yield: 74.6%. Anal. Calcd. for $[C_{43}H_{34}CoN_4O_6P] \cdot 3H_2O$:C, 63.39; H, 4.95; N, 6.88%. Found: C, 63.98; H, 4.53; N, 6.72%. FT-IR (KBr pellet): 3461 (s), 3064 (w), 2938 (w), 2919 (w), 2857 (w), 1675 (s), 1643 (s), 1627 (s), 1382 (m), 1330 (m) cm^{-1}. ESI-MS: 421 m/z (negative ion mode). UV–Vis: $\lambda_{max} = 532$ nm, $\varepsilon = 1.846 \times 10^3$ L mol^{-1} cm^{-1}.

2.3 Synthesis of Co(III) Catalyst and Carbon Nanomaterial Composite

Co(III) complex (**2**) was mixed with graphene to form desired ratio of catalyst to nanomaterial and sonicated in methanol (1 mg/mL) for 30 min. Then, 40 μL of Nafion® was added to the solution and sonication resumed for an additional 30 min. After drop-casting 10 μL onto a polished glassy carbon electrode, the electrode was allowed to dry and this served as the catalyst for ORR studies.

2.4 Electrochemical Studies

A standard three electrode electrochemistry setup, including a glassy carbon working electrode coated with the nanocomposite, a platinum counter electrode, and an Ag/AgCl reference electrode, was used in the collection of data. When reporting the ORR peak potentials, all values were converted to SHE reference electrode. Studies were carried out in phosphate buffer solutions, and these were purged with either O_2 or N_2 gas for at least 1 h prior to use. CV, RDE, and RRDE studies were performed in order to establish and assess the capability of the material to perform ORR and the mechanism. The sequence of CV studies performed were as follows. Initially, studies were undertaken to determine which peaks were attributable to ORR in acidic and basic conditions. Following this, nanomaterial studies were used to determine which material produced the best ORR results, and pH studies were then investigated to find optimal conditions. Various pH levels were examined, including pH 2, 4, 7, and 9.

3 Results and Discussion

3.1 Characterization of Co(III) Catalyst and Co-Graphene Nanocomposite

FT-IR spectrum of **2** is provided in Figure S3 (Supporting Information). This spectrum is compared with a previously published spectrum of the amidomacrocyclic ligand [40]. C–H stretching in **2** is evident between 3064 and 2857 cm^{-1}, slightly shifted from 2967 to 2852 cm^{-1} in **1**, as well as an amide C=O stretching frequency present at 1643 cm^{-1} in **2** shifted from 1668 cm^{-1} in **1** and an amide C–N stretch at 1330 cm^{-1} in **2** shifted from 1294 cm^{-1} in **1**. A noteworthy feature in the spectrum of **2** includes the absence of the amide N–H peak at 3259 cm^{-1}. ESI-MS was performed on **2** (molecular weight 421.3 g mol^{-1}) and a major peak emerged at 421 m/z (negative ion mode); this is presented in Figure S4 (Supporting Information) along with an inset graph of theoretical isotope distribution. UV–Vis of **2**, presented in Figure S5 (Supporting Information), shows that the $\lambda_{max} = 532$ nm, at which point the absorbance is 0.208 at a concentration of 1.13×10^{-4} M and the calculated molar absorptivity value is $\varepsilon = 1.85 \times 10^3$ L mol^{-1} cm^{-1}.

SEM imaging of the graphene-supported Co(III) complex, given in Figure S6 (Supporting Information), indicates that the graphene nanomaterial exists morphologically as crinkled sheets with no visible stacking. This is consistent with previous observations made regarding a separate Co(III) composite material, which was also employed for ORR [39]. TEM imaging of the nanocomposite was also performed to characterize in depth the morphology of **2** supported on graphene, and this analysis is given in Supporting Information Figure S7 (Supporting Information). The end of a crinkled graphene sheet is observable in much greater detail (Figure S7a) and appears to consist of around 20 layers at one section of the sheet. Also, there is evidence of a thin coating which can be seen at the very edges of another graphene sheet when viewed from the top (Figure S7b), and this may be attributed to a thin layer of catalyst atop the nanomaterial. In order to further confirm the presence of **2** upon the graphene, STEM with EDS was performed to analyze the distribution of cobalt, along with catalyst-derived heteroatoms, upon the nanocarbon framework. According to the elemental mapping from EDS of a STEM parent image, the four key elements Co, carbon (C), nitrogen (N), and oxygen (O) present in **2** are evenly dispersed across and throughout the graphene nanomaterial. This evidence of good catalyst dispersion in graphene nanomaterial confirms that the non-stacked morphology found in SEM is beneficial for the loading of catalyst upon the graphene sheets, and this consequently allows oxygen better access to active sites, optimally facilitating ORR. The STEM with EDS images are given in Fig. 2, with the parent image also provided for context.

In order to gain more insight into the chemical state and structure of the graphene nanomaterial, XRD was performed. There are two major diffraction peaks, which appear at 2θ equal to 25.7° and 43.0°, respectively (Figure S8, Supporting Information). The first peak at 25.7° corresponds to reduced graphene oxide, which approximates pristine graphene [45]. The second, smaller peak at 43.0° is indicative of the turbostratic band of disordered carbon materials, meaning that to some extent the material is amorphous in character, as evidenced by the SEM imagery of crinkled sheets [46]. The marked absence of a peak between 10° and 11° serves to confirm that there is an undetectable amount of graphene oxide present [47]. Therefore, as intended, the simple mixing and sonication deposition of **2** upon the graphene framework neither oxidized the graphene nor covalently attached to the nanomaterial. XRD analysis also allows for calculation of the interlayer distance between atomic sheets in the material. The peak at 25.7° corresponds to an interlayer distance of 3.5 Å while the peak at 43.0° has a distance value of 2.1 Å. XPS analyses were
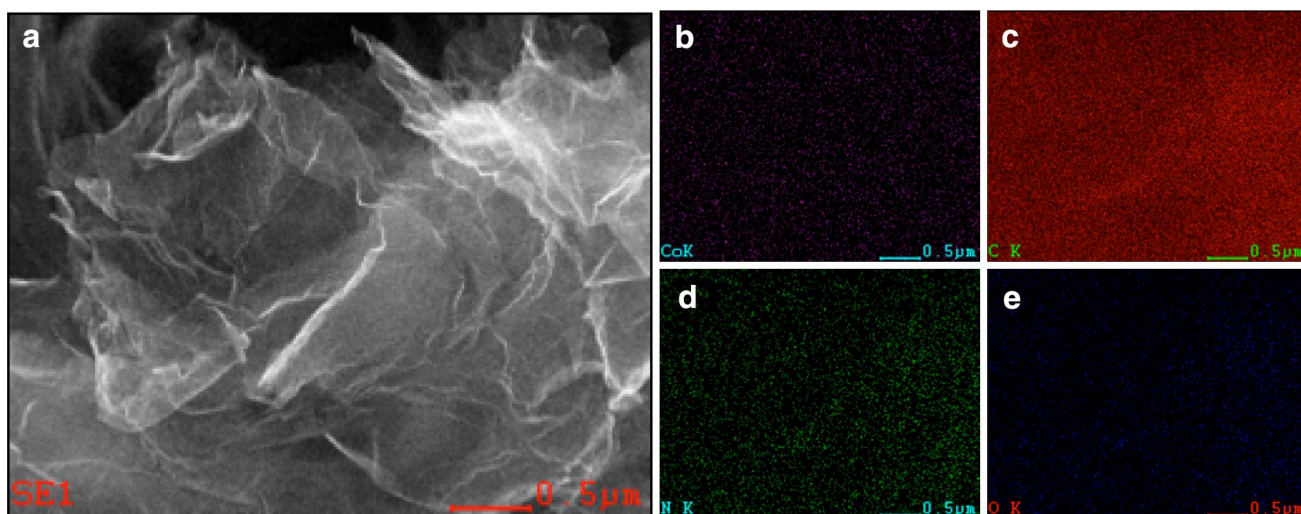
Fig. 2 **a** STEM of the Co-graphene nanocomposite with EDS of **b** Co, **c** C, **d** N, and **e** O in the sample

performed for the nanocomposite to determine the state of the major elements found in the material, including Co, C, N, and O. A survey scan was performed followed by narrow scans of the four main elements found in the nanocomposite (Fig. 3). The binding energy of the C1s narrow scan (Figure S9, Supporting Information) was set to 284.0 eV for sp^2

carbon bonds found in the graphene nanomaterial [48]. The Co2p spectrum (Fig. 3b) demonstrates spin–orbit splitting of precisely 15 eV between the two parents peaks at 779.9 and 794.9 eV, confirming that the Co in the sample primarily exists as Co(III) rather than Co(II) [49, 50]. The three sets of satellite peaks originate from possible photoreduction of the
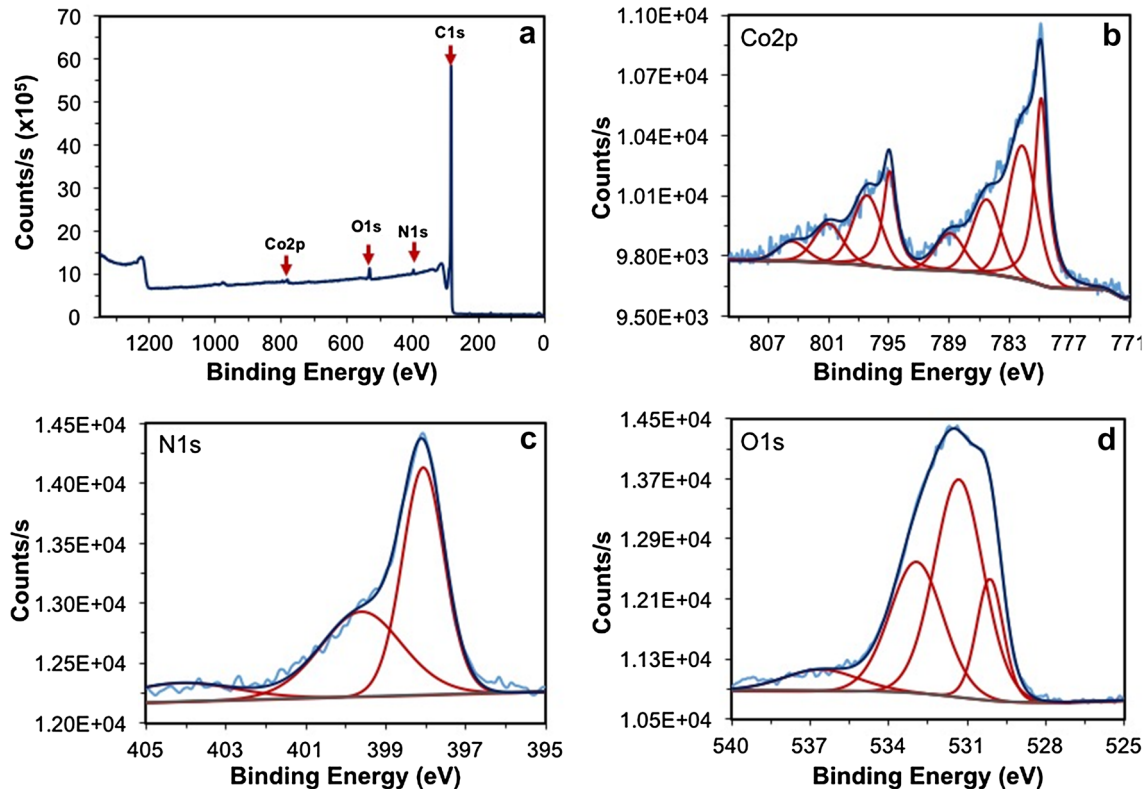
Fig. 3 XPS scans of Co(III)-graphene nanocomposite **a** survey scan, **b** Co2p narrow scan, **c** N1s narrow scan, and **d** O1s narrow scan

Co(III) catalyst to Co(II) by X-ray during XPS analysis. This phenomenon is possible due to electron transfer from the four electron-rich deprotonated amide groups in the ligand to the metal center [51]. Peak binding energy values are tabulated in Table S1 (Supporting Information). The narrow scan of N1s gave two major peaks with binding energies of 398.1 and 399.6 eV (Fig. 3c), which is indicative of the amide nitrogen groups found in **2** and the electronic interaction between these amide nitrogens and the carbons in the graphene, respectively [52, 53]. The O1s binding energy peak at 530.1 eV is associated with the carbonyl oxygens found in **2** (Fig. 3d) [54].

3.2 CV Studies of Co-Graphene Composites

Figure 4 demonstrates the capability of Co(III)–graphene nanocomposite to perform ORR. The peak potential at −0.088 V (versus SHE) is observed under acidic conditions (pH 2) in the presence of O_2, and no peak is observed in this location when the same parameters are tested in N_2-flushed solution. This serves to confirm that the reaction indicated is, indeed, ORR. Similar trials were conducted for pH 9 due to the presence of what appears to be a pseudo-reversible redox process centered around −0.243 V (versus SHE) in addition to the ORR peak which appears at −0.067 V (versus SHE). Comparison of aerobic and anaerobic conditions confirms that the prominent peak at −0.067 V (versus SHE) is due to ORR, as it does not appear in the absence of O_2. Furthermore, the redox process is still found to occur in N_2-flushed conditions, indicating that it is due to the material itself. The oxidation state of the Co complex can possibly be oxidized to a high-valent state during this process and cause a redox to occur in this region [55]. When compared to a commercial 20 wt% Pt/C electrode, a small reduction peak around 37 mV (versus SHE) is observed albeit at a much smaller current density compared to the Co-graphene nanocomposite (Figure S10). We would also like to mention that oxygen

reduction peak in the nanocomposite is much more defined with greater area under the curve than Pt/C. An oxidation peak can be found in the Pt/C voltammogram at −88 mV (versus SHE), which has been observed previously [56].

Both graphene and MWCNTs were investigated as sources of nanocarbon supports for developing a composite with **2**. As seen in Fig. 5, MWCNT-supported complex was found to reduce O_2 at a peak potential 155 mV higher than the graphene-supported complex. However, the current density of the ORR facilitated by the Co-graphene nanocomposite was over two times greater in terms of current density, potentially due to the non-stacked graphene sheets which provided greater surface area (and therefore greater access to active sites) than the MWCNT composite, which is comprised of multiple carbon nanotubes tightly packed within one another [57]. Based on the results of the nanomaterial study, while MWCNTs indicated decreased overpotential towards ORR, the graphene-supported nanocomposite reduced a larger amount (concentration) of oxygen as indicated by the significant increase in current density.
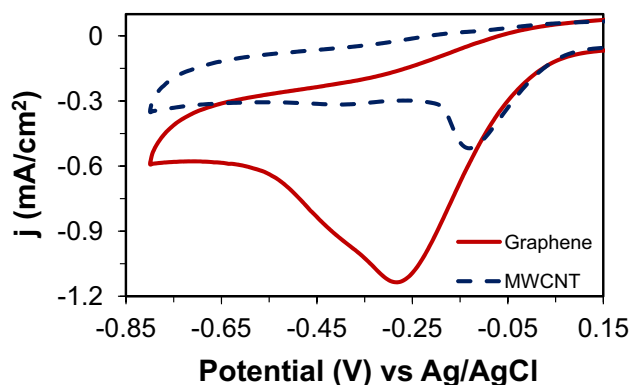
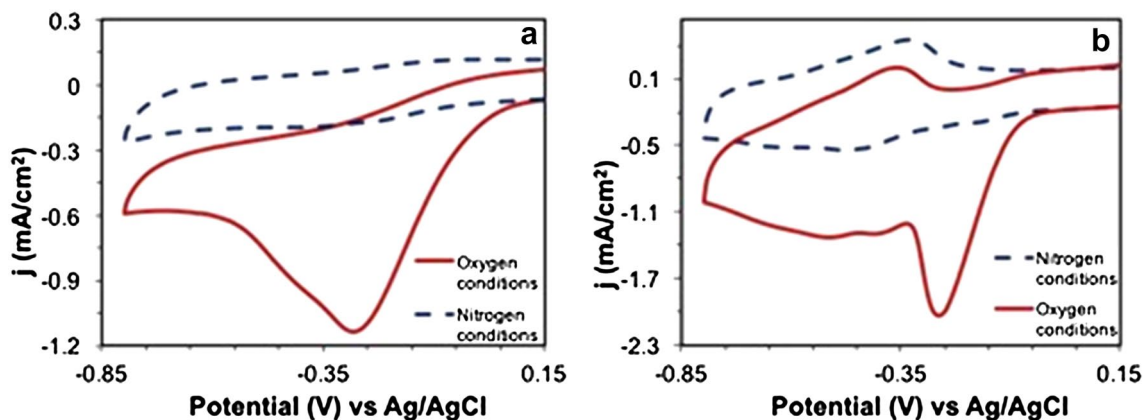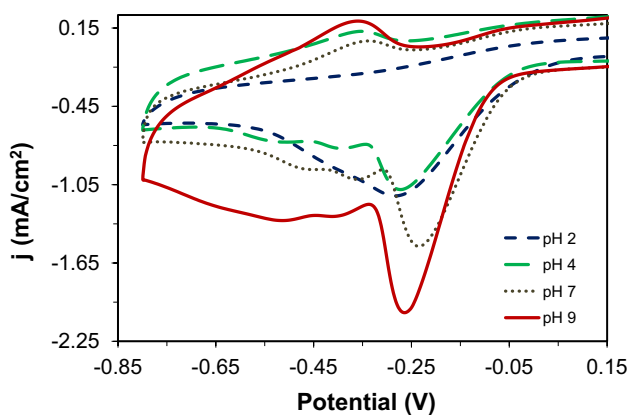**Fig. 5** CV of graphene-supported and MWCNT-supported catalyst composite materials

Fig. 4 CV of Co-graphene nanocomposite at **a** pH 2 and **b** pH 9 in O_2- and N_2-flushed solutions

Fig. 6 CV of Co-graphene nanocomposite performing ORR in different pH conditions

Subsequent studies were performed using graphene-based composite materials.

In order to assess the capability of the Co-graphene nanocomposite to perform ORR in a variety of environments, a range of pH studies were performed. The previously given CV data was collected at pH 2, under which conditions the ORR peak appears at -0.088 V (versus SHE), and at pH 9, the ORR peak appears at -0.067 V (versus SHE). Additional pH 4 and pH 7 conditions were investigated, and the ORR activity in all four environments is given in Fig. 6. While alkaline conditions (pH 9) are found to yield the best current density, which is found to be 2.03 mA cm^{-2}, neutral conditions (pH 7) produce the highest peak potential, at a value of -0.033 V (versus SHE). ORR at pH 4 and pH 2 is found to occur at a similar current density and peak potential, with pH 4 conditions producing a slightly better peak potential but with slightly less current density. It may also be noted that the redox process formerly observed in alkaline conditions, and absent at pH 2, also appears at pH 4 and pH 7 conditions.

3.3 RDE and RRDE Studies

RDE studies were performed for the nanocomposite in order to determine the number of electrons associated with ORR. Under acidic conditions, oxygen may be reduced to water in a one step, four-electron process; however, in some instances oxygen may be reduced to hydrogen peroxide via a two-electron exchange. While the reduction of oxygen to hydrogen peroxide is an also an ORR process, the production of peroxide is undesirable due to its oxidative character which degrades the catalyst, lowering its ORR activity. Figure S11a (Supporting Information) shows RDE data collected at pH 2 at various rotating speeds. In order to determine the number of electrons involved in this electrochemical process, the convective movement between analyte solution

and electrode surface is related mathematically using the Koutecky–Levich equation, in which the Levich current (J_{Lev} = $0.620nFCD^{2/3}\omega^{1/2}v^{-1/6}$ where n = number of electrons transferred, F = Faraday constant, C = molar concentration of analyte, D = diffusion coefficient at 25 °C, ω = angular rotation rate of the electrode, and v = kinematic viscosity of the solution at 25 °C) is related to the kinetic current (J_K) and the observed limiting currents (J_{lim}) from experimental RDE data. These are used to construct the Koutecky–Levich equation:

$$J_{lim}^{-1} = J_{Lev}^{-1} + J_{K}^{-1} \qquad (1)$$

The slope of J_{Lev} was obtained by plotting the graph between J_{lim}^{-1} and $\omega^{-1/2}$. The resultant Koutecky–Levich plot is presented in Figure S11b (Supporting Information), in which experimental data is fitted with a trendline and compared with theoretical four-electron and two-electron process. Results indicate that at pH 2 the nanocomposite performs ORR through a 3.60 electron process. From J_K and the number of electrons we can calculate the rate constant of ORR using Eq. 2, where k is the rate constant and Γ is the concentration of the catalyst on the electrode surface. In acidic conditions, the rate constant was determined to be 9.78×10^6 mol^{-1} s^{-1}. RRDE was used to verify the results obtained from RDE, and the results are presented in Fig. 7, in which the number of electrons associated with ORR was determined to be 4.05 further confirming a four-electron process.

$$J_K = 10^3 nFkC\Gamma \qquad (2)$$

RDE and RRDE were additionally performed at pH 9 to evaluate the ORR mechanism in alkaline conditions, and the results also indicate a four-electron process. The mechanism involves 3.86 electrons at pH 9 based on RDE and Koutecky–Levich plots, given in Fig. 8, and the rate constant is calculated to be 2.58×10^5 mol^{-1} s^{-1}. The RRDE data is
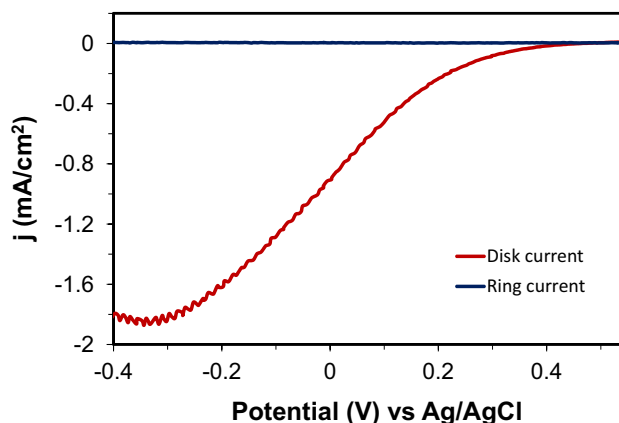
Fig. 7 RRDE of Co(III) complex supported on graphene collected at pH 2 and 1600 rpm
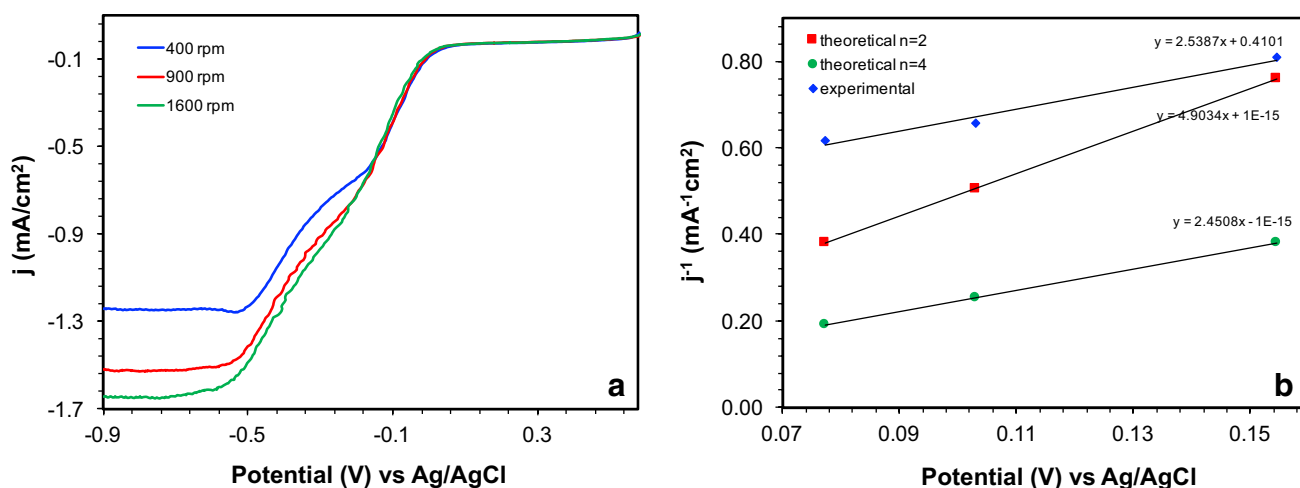
Fig. 8 **a** RDE of Co(III) complex supported on graphene at pH 9 and **b** Koutecky–Levich plot of RDE data collected at pH 9

presented in Figure S12 (Supporting Information) and confirms the four-electron mechanism in alkaline conditions, with 4.18 electrons calculated from the RRDE equation:

$$n = 4 \left[i_d / \left(i_d + i_r N_C^{-1} \right) \right] \qquad (3)$$

where n is the number of electrons involved in the mechanism, N_C represents RRDE collection efficiency, a constant based on the electrode, and i_d and i_r represent the disk current and ring current, respectively. The performance of the Co-graphene nanocomposite is compared with that of other recent cobalt catalysts for ORR in Table 1 based on calculated electrons involved in the mechanism as well as rate constant and ORR peak potential versus SHE.

Previously prepared Co-MWCNT nanocomposite performed ORR at a peak potential approximately 131 mV higher than the Co-graphene nanocomposite, and although the calculated electron transfer numbers were both close to 4, the rate constant for the prepared Co-graphene nanocomposite is nearly two orders of magnitude higher [38]. For comparison, the Co-MWCNT composite prepared and presented in Sect. 3.2 outperforms the referenced

MWCNT nanocomposite, with a peak potential 24 mV higher for ORR. A very similar Co-catalyst composite which includes two chloro groups on the ligand performs at a significantly greater (+ 325 mV) ORR peak potential, yet the rate constant of the prepared Co-graphene nanocomposite is far higher in this instance as well [39]. Cobalt complexes with nanocarbon fibers and cobalt core/cobalt oxide shell nanoparticles embedded in pyrolyzed polydopamine had similar calculated electron numbers to the presented Co-graphene nanocomposite, and the ORR peak potentials were only slightly higher [57, 58]. Compared to a cobalt porphyrin complex supported on nanotubes, the Co-graphene nanocomposite has a lower ORR peak potential yet a rate constant over five times higher [59]. Overall, while the peak potential of ORR is lower than many comparable cobalt catalyst systems for the prepared Co-graphene nanocomposite, the number of electrons involved in the mechanism is indicative of the most desirable reduction pathway and the rate constant of this reaction is higher, often much more so, than reported values for many other materials.

Table 1 Comparison of prepared composite performance versus other recent cobalt catalysts for ORR

Cobalt catalyst	Electron number	Rate constant ($mol^{-1}s^{-1}$)	Peak potential (V) of ORR (vs. SHE)	Reference
$Co_3(PO_4)_2 \cdot 4H_2O$	3.50–3.60	–	0.7	[25]
Co-MWCNT	3.95	1.62×10^5	0.043	[38]
Di-chloro Co-graphene	4.04	3.85×10^5	0.237	[39]
Co-NCF	3.96	–	0.027	[55]
$Co@Co_3O_4@PPD$	3.96	–	− 0.027	[58]
Co-porphyrin-CNT	4.2	1.8×10^6	0.447	[59]
Co-graphene	3.60	9.78×10^6	− 0.088	This work

## 3.4 Proposed General Mechanism

Based on the results from RDE and RRDE studies, it can be concluded that the mechanism via which the material is performing ORR is a four-electron process (Fig. 9), as opposed to a two-electron process, in both acidic and alkaline conditions as determined by electrochemical studies at pH 2 and 9, respectively. XPS results confirm presence of Co(III) species in the nanocomposite, and during ORR, a high-valent oxidation state is likely achieved by the Co center upon initial binding of an O_2 molecule. Reduction of the O_2 to water regenerates the original Co(III) oxidation state and completes the catalytic cycle in acidic conditions [38]. In alkaline conditions, the greater concentration of hydroxide ions likely causes the mechanism to proceed through an alternative pathway in which the Co(III) center forms an unstable hydroperoxo intermediate with O_2 and water that quickly reduces to hydroxide, regenerating the Co(III) and completing the catalytic cycle [39, 60].

4 Conclusion

Here, we have reported for the first time both the synthesis of a Co(III) amidomacrocyclic complex and its application towards ORR. Graphene was chosen as a nanocarbon support for the catalyst and the resultant material was evaluated electrochemically in acidic and alkaline conditions. CV demonstrated the capability of the material to perform ORR at a peak potential of -0.088 V (versus SHE) in pH 2 conditions, at -0.067 V (versus SHE) in pH 9 conditions, and that this performance is enhanced when using graphene rather than MWCNTs. The mechanism was determined to proceed through the desired four-electron pathway involving direct reduction of oxygen to water in acidic conditions, with 3.60 and 4.05 electrons calculated, respectively, from RDE and RRDE at pH 2. Alkaline conditions also enabled the material to proceed through this mechanism, although the observed rate constant of 9.78×10^6 mol^{-1} s^{-1} in acidic conditions was greater than the rate constant calculated for pH 9. Due to these results, it may be concluded that this novel material has great potential for application as a more cost effective platinum alternative to be used in commercialization of PEMFCs.

Fig. 9 Proposed mechanism of oxygen reduction via Co(III) complex/graphene nanocomposite in acidic and alkaline conditions
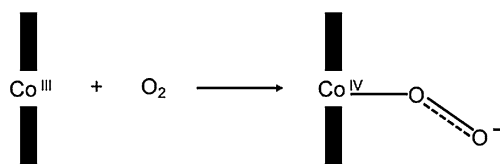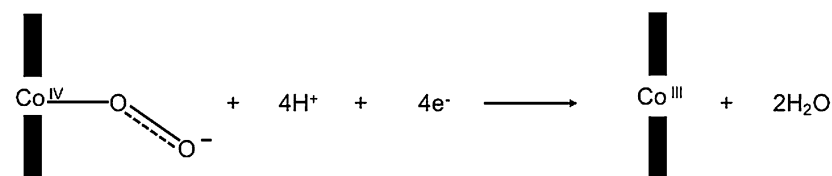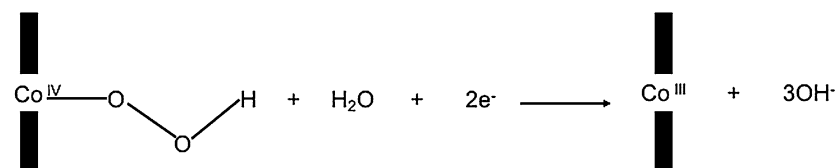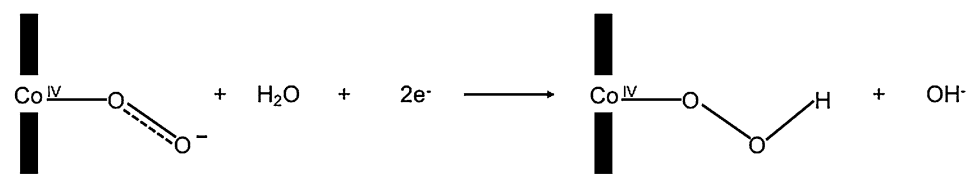
References

1. Jewulski JR, Rak ZS (2006) Environ Prot Eng 32:189
2. Li X (2007) In: Zhao TS (ed) Advances in fuel cells, vol 1, chap 1. Elsevier, Oxford
3. Cooper HW (2007) Chem Eng Prog 103:34
4. Kohnke HJ (2011) Chem Ing Tech 83:2027
5. Rasmussen M, Abdellaoui S, Minteer SD (2016) Biosens Bioelectron 76:91
6. Afif A, Radenahmad N, Cheok Q, Shams S, Kim JH, Azad AK (2016) Renew Sustain Energ Rev 60:822
7. Mathuriya AS, Yakhmi JV (2016) Crit Rev Microbiol 42:127
8. Wasmus S, Kuver A (1999) J Electroanal Chem 461:14
9. Akhairi MA, Kamarudin SK (2016) Int J Hydrogen Energy 41:4241
10. Gerasimov GY (2015) J Eng Phys Thermophys 88:1498
11. Ozoemena KI (2016) RSC Adv 6:89523
12. Winter M, Brodd RJ (2004) Chem Rev 104:4245
13. Cheng X, Shi Z, Glass N, Zhang L, Zhang J, Song D, Liu Z, Wang H, Shen J (2007) J Power Sources 165:739
14. Ho JC, Saw E, Lu LYY, Liu JS (2013) Technol Forecast Soc Change 82:66
15. Ravinshankara AR, Rudich Y, Pyle JA (2015) Chem Rev 115:3679
16. Sealy C (2008) Mater Today, 11:65
17. Chen Z, Higgins D, Yu A, Zhang L, Zhang J (2011) Energy Environ Sci 4:3167
18. Higgins DC, Chen A (2013) Can J Chem Eng 91:1881
19. Reshetenko TV, St-Pierre J (2016) J Power Sources 333:237
20. Awad MI, Saleh MM, Oshaka T (2011) J Power Sources 196:3722
21. Tang Y, Yang Z, Dai X (2012) J Nanopart Res 14:844:1
22. Yang Z, Nakashima N (2015) Sci Rep 5:1
23. Osgood H, Devaguptapu SV, Xu H, Cho J, Wu G (2016) Nano Today, 11:601
24. Mathur A, Kushwaha HS, Vaish R, Halder A (2016) RSC Adv 6:94826
25. Zhan Y, Lu M, Yang S, Xu C, Liu Z, Lee JY (2016) ChemCatChem 8:372
26. Liu C, Li G, Cheng G, Hao C, Chen S, Xie Y (2016) RSC Adv 6:73581
27. Song T, Wang D, Wang H, Li X, Liang Y, Xie J (2015) Int J Hydrogen Energy 40:3868
28. Sarapun A, Samolberg L, Kreek K, Kowl M, Matisen L, Tammeveski K (2015) J Electroanal Chem 746:9
29. Levy N, Mahammed A, Friedman A, Gavriel B, Gross Z, Elbaz L (2016) ChemCatChem 8:1
30. Zagal JH, Koper MTM (2016) Angew Chem Int Ed 55:2
31. Turk KK, Kruusenberg I, Mondal J, Rauwel P, Kozlova J, Matisen L, Sammelselg V, Tammeveski K (2015) J Electroanal Chem 756:69
32. Wang C, Waje M, Wang X, Tang JM, Haddon RC, Yan Y (2004) Nano Lett 4:345
33. Wang Y, Fang B, Li H, Bi XT (2016) Prog Mater Sci 83:445
34. Lam E, Luong JHT (2014) ACS Catal 4:3393
35. Seger B, Kamat PV (2009) J Phys Chem 113:7990
36. Wang X, Li W, Chen Z, Waje M, Yan Y (2006) J Power Sources 158:154
37. Hayden BE, Pletcher D, Suchsland JP, Williams LJ (2009) Phys Chem Chem Phys 11:9141
38. Nasini UB, Gartia Y, Ramidi P, Kazi A, Shaikh AU, Ghosh A (2013) Chem Phys Lett 566:38
39. Gartia Y, Parnell CM, Watanabe F, Szwedo P, Biris AS, Peddi N, Nima ZA, Ghosh A (2015) ACS Sustain Chem Eng 3:97
40. Parnell CM, Chhetri B, Brandt A, Watanabe F, Nima ZA, Mudalige TK, Biris AS, Ghosh A (2016) Sci Rep 6:31415
41. Sullivan SZ, Ghosh A, Biris AS, Pulla S, Brezden AM, Collom SL, Woods RM, Munshi P, Schnackenberg L, Pierce BS, Kannarpady GK (2010) Chem Phys Lett 498:359
42. Ghosh A, Sullivan SZ, Collom SL, Pulla S (2014) US Patent No 8722881:B2
43. Carmody WR (1961) J Chem Ed 38:559
44. Ghosh A, Ramidi P, Pulla S, Sullivan SZ, Collom SL, Gartia Y, Munshi P, Biris AS, Noll BC, Berry BC (2010) Catal Lett 137:1
45. Xu ZW, Huang YD, Min CY, Chen L (2010) Radiat Phys Chem 79:8
46. Chang BYS, Huang NM, An'amt MN, Marlinda AR, Norazriena Y, Muhamad MR, Harrison I, Lim HN, Chia CH (2012) Int J Nanomed 7:3379
47. Gurunathan S, Han JW, Dayem AA, Eppakayala V, Kim J (2012) Int J Nanomed 7:5901
48. Miller DJ, Biesinger MC, McIntyre NS (2002) Surf Interface Anal 33:299
49. Chuang TJ, Brundle CR, Rice DW (1976) Chem Ing Tech 59:413
50. Biesinger MC, Payne BP, Grosvenor AP, Lau LWM, Gerson AR, Smart RSC (2011) Appl Surf Sci 257:2717
51. Truica-Marasescu F, Wertheimer MR (2008) Plasma Process Polym 5:44
52. Krussenberg I, Matisen L, Tammeveski K (2013) J Electrochem Sci 8:1057
53. Parnell CM, Watanabe F, Nasini UB, Berry BC, Mitchell T, Shaikh AU, Ghosh A (2015) J Electroanal Chem 740:37
54. Lopez GP, Castner DG, Ratner BD (1991) Surf Interface Anal 17:267
55. Yan J, Lu H, Huang Y, Fu J, Mo S, Wei C, Miao Y, Liu T (2015) J Mater Chem A 3:23299
56. Kim JR, Kim J-Y, Han S-B, Park K-W, Saratale GD, Oh S-E (2011) Bioresour Technol 102:342
57. Chen D, Tang L, Li J (2010) Chem Soc Rev 39:3157
58. Wang Z, Li B, Ge X, Goh FWT, Zhang X, Du G, Wuu D, Liu Z, Hor TSA, Zhang H, Zong Y (2016) Small 12:2580
59. Zhang W, Shaikh AU, Tsui EY, Swager TM (2009) Chem Mater 21:3234
60. Song C, Zhang J (2008) In: Zhang J (ed) PEM fuel cell electrocatalysts and catalyst layers, chap. 5. Springer, London.